IEEE Access
Multidisciplinary | Rapid Review | Open Access Journal

Received October 21, 2019, accepted November 2, 2019, date of publication November 11, 2019,
date of current version November 20, 2019.

Digital Object Identifier 10.1109/ACCESS.2019.2952740

Visualizing and Quantifying Thoraco-Abdominal Asynchrony in Children From Motion Point Clouds: A Pilot Study

HAYTHEM REHOUMA[1], (Member, IEEE), RITA NOUMEIR[1], (Member, IEEE), GABRIEL MASSON[2], SANDRINE ESSOURI[2], AND PHILIPPE JOUVET[2]

[1]École de Technologie Supérieure, Montréal, QC H3C 1K3, Canada
[2]CHU Sainte-Justine, Mother and Child University Hospital Center, Montréal, QC H3T 1C5, Canada

Corresponding author: Haythem Rehouma (haythem.rehouma.1@ens.etsmtl.ca)

This work was supported in part by the Natural Science and Engineering Research Council of Canada (NSERC), and in part by the Institut de valorisation des données (IVADO).

ABSTRACT In a situation of respiratory failure (RF), patients show signs of increased work of breathing leading to the involvement of accessory respiratory muscles and a desynchronization between rib cage and abdomen known as thoraco-abdominal asynchrony (TAA). Proper assessment of these signs requires sufficiently skilled and trained medical staff. However, human assessment is subjective and is practically impossible to audit. A new non-contact method is proposed for TAA visualization and quantification, in children with RF. The surface variations are analyzed by calculating the 3-dimensional motion of the thorax and abdomen regions during the breathing process. A high-fidelity mannequin was used to simulate thoraco-abdominal asynchrony. The proposed system uses depth information recorded by an RGB-D (Red Green Blue-Depth) camera. Furthermore, surface displacement was calculated in four simulated modes from the normal to the severe TAA mode. Respiratory rates were also calculated based on the analysis of the surface movements. The proposed method was compared to a highly precise laser-ranging system with 1 mm resolution. The resulting root mean square deviation (RMSD) showed an error of 1.78 ml in normal mode, 2.83 mm in mild mode, 2.23 mm in severe mode and 2.34 mm in irregular mode. The results showed a high correlation between the two methods in estimating the retraction distance and respiratory rate ($\rho > 0.985$).

INDEX TERMS Non-contact breathing monitoring, clinical environment, motion estimation, quantitative measures, respiratory failure, sensors, thoraco-abdominal asynchrony (TAA), spontaneous breathing.

I. INTRODUCTION

In a clinical environment, breathing monitoring is an important vital task that is done on a daily basis for patients of all ages. Breathing monitoring mainly comprises an assessment of the chest wall motion and the measurement of physiological signs such as respiratory rate and tidal volume. While many methods have been developed for physiological parameters assessment, there is still a lack of methods to better assess the chest wall spatial motion in spontaneous breathing patients.

Chest wall motion assessment, in clinical practice, is currently based on intermittent human observation of the rib cage and abdominal compartments and is done through physical examinations. In fact, visual inspection is the first tool in physical examinations. This initial assessment allows the early detection of a potential respiratory failure in order to provide the appropriate medical treatment to the patient. In case of respiratory failure, determining the severity is a key factor to help the clinician to make the right decision, whether by providing an immediate oxygen support and possibly bag-and-mask ventilation or even patient intubation and mechanical ventilation to provide full or partial breathing support.

Chest wall distortion, known as thoraco-abdominal asynchrony or paradoxical motion, is one of the most important clinical symptoms of respiratory failure [1]–[3]. This clinical sign is visually inspected by the physician. However, the accuracy of this inspection is highly correlated to the clinician's expertise. The interpretations of a patient's results are thus, limited by high inter-observer variation.

The associate editor coordinating the review of this manuscript and approving it for publication was Mauro Fadda.

This subjectivity is problematic, especially when healthcare resources such as pediatric experts are limited. Objective assessment of chest wall motion, on the other hand, is difficult because there are no standard medical devices reporting quantitative values of the surface displacements to address the severity of patients' symptoms when the paradoxical motion occurs.

Previous works aimed at quantifying the chest wall movement and detecting the thoracoabdominal asynchrony, generally make use of respiratory inductive plethysmography [4]–[7]. This contact method requires surrounding the subject with two belts, one thoracic and one abdominal. Although the results are reasonably good, the application of this technique is still limited by some unresolved issues such as the calibration process and the restrictions of contact with the subject's body. Moreover, contact-based methods may create discomfort to the patient and influence his breathing, an effect which is more pronounced in infants.

In this work, we present a contactless real-time imaging system designed to monitor and observe the most active regions on the thoraco-abdominal surface through a 3D imaging measurement method. The proposed system visualizes deformations of the chest wall through a 3D imaging measurement method, allowing the detection of two parallel pathways of the body wall motion when thoraco-abdominal movements (TAM) occurs. Furthermore, the thorax and abdomen regions were individually analyzed to quantify the thorax-to-abdomen breathing displacement. Using an RGB-D sensor, geometric information (depth data) and intensity variations (color images) are utilized together to estimate a dense 3D motion field.

The proposed system uses a coarse-to fine multiresolution approach to represent different levels of displacement estimation. The estimation is an optimization problem that is solved based on a primal-dual approximation framework. Using the cloud-to-cloud distance estimation, displacement distances were calculated between thoracic and abdominal regions. Experiments were conducted in four simulated retraction modes from the normal to the severe mode.

II. RELATED WORKS

Various techniques have been proposed for chest wall motion assessment, as shown in Table 1. These techniques can be grouped into two main classes: contact and non-contact. In contact methods, chest wall motion has been measured using sensing devices attached to the subject's body; these include magnetometers [8], [9] and respiratory inductive plethysmography [4]–[7].

For non-contact techniques, many works have been proposed using different types of techniques, including optoelectronic plethysmography (OEP) [10]–[14], electromagnetic devices and radiological techniques [15], [16]. Two major shortcomings of OEP-based approaches are that they require particular skills to be used effectively [17], and they utilize a huge number of markers [18], [19], requiring complex and slow preparations and thus, may be uncomfortable for patients, especially infants [17], [20]. Meanwhile, radiological techniques present higher cost, slow acquisition, low resolution and high noise levels, and they may cause patient exposure to an extra dose of radiation [21]–[24]. Additionally, the need to be inside a scanner for long periods limits these approaches and makes their application especially difficult when managing certain groups of patients such as children, newborns, the elderly and patients with acute diseases.

In order to overcome those limitations, researchers have investigated optical techniques in more depth, taking advantage of the rapid progress in scene understanding using the new RGB-D cameras [25] that has provided a way to explore new computer vision approaches for respiration assessment. These algorithms go from a general investigation of breathing waveforms [26], [27] to the estimation of respiratory rates [28], [29] and lung volumes [30], [31], which are part of respiration physiological assessment. Physiological parameters estimation has been studied in our previous work [32].

Chest wall motion assessment using RGB-D cameras utilizes a light source with various projection patterns to extract the desired information from the measured surface. This assessment process using RGB-D cameras can be grouped into two main categories : structured-light (SL) based techniques [26], [33]–[35] and time-of-flight (TOF) based techniques [31], [36]–[39].

For example, Aoki *et al.* [26] proposed a contactless method using an SL camera to compute respiration waveforms during a bicycle pedaling exercise. In their method, a region of interest (ROI) is extracted using the depth information, and then a second region where the respiration component is more dominant than the pedaling motion component is extracted from the ROI by applying a Fourier Transform (FT) Band Pass Filter (BPF). The respiration waveform is finally calculated using a frequency analysis of the depth changes between the frames in the region of respiration. Although their results showed good correlation with an expiration gas analyzer, their study was very limited, and the authors provided no further details. Seppanen *et al.* [33] generated respiratory airflow waveforms using an SL depth sensor. They reported a good correlation between the estimated airflow signal and a spirometer signal, used as a gold standard method. Tahavori *et al.* [22] investigated the motion data variance due to breathing. The authors used an SL depth camera, which they placed above the body to calculate the average depth value of 16 ROIs on the chest and abdomen surfaces to analyze their motion over time. They demonstrated that after applying the principal component analysis (PCA) to the calculated average depth values, the first principal component already describes more than 70% of the motion data variance in thoracic and abdominal surfaces.

Povšič et al. proposed a method for respiration displacement visualization in the thoraco-abdominal region [34]. Their results showed that the proposed approach is accurate and comparable to the Iterative Closest Point (ICP) method, used as a reference method. The technique can be a useful

TABLE 1. A comparative overview of the differences between previous methods in respiratory assessment.

Method /device	Author name, year	Measured parameter	Validation method, validation dataset	Results with respect to each study's objective
OEP	Dellaca et al., 2010 [17]	Chest wall volume changes	Pneumotachograph, s=20 newborns	• $r^2 = 0.95$
	Aliverti et al., 2000 [19]	Chest wall volume changes	Spirometry and pneumotachography, s= 24	• $d1$ =1.7 ± 5.9% • $d2$ =-1.6. ± 5.4% • $d3$ =4.9 ± 6.4%
	Reinaux et al., 2016 [20]	Tidal breathing measurements	Pneumotachograph, s=20 infants	• mean difference =0.02 ml • limit of agreement from 4.11 to 4.08 ml (95%CI)
ToF Sensor	Soleimani et al., 2017 [30]	Forced vital capacity	Spirometer, s=85	• $r^2 = 0.98$
	Ulrich et al., 2010 [36]	Respiratory motion	Reference signals used as ground truth, s=0 (using a phantom)	• for a breathing amplitude of 1.5 mm: $\rho = 0.65$ • for a breathing amplitude bigger than 5 mm: $\rho > 0.8$
	Penne et al., 2008 [37]	Respiratory signal	Respiratory gating System ANZAI belt (AZ733V, ANZAI Medical Co.), s=13	• $\rho = 0.85$ (chest) • $\rho = 0.91$(abdomen)
	Ostadabbas et al., 2015 [44]	Airway resistance	Clinical results using spirometry and plethysmography tests, s=14	• tidal volume error= 0.07±0.06 liter • accuracy in predicting three levels of severity of airway obstruction =76.2% • accuracy of airway obstruction detection = 80%
	Procházka et al., 2016 [45]	Respiratory rate	Contact-based sensor (Garmin Ltd), s=1	• accuracy = 0.26%
SL 3D sensor	Tahavori et al., 2014 [22]	Respiratory motion (investigate dominate variations) using PCA	Multi-ROI analysis, s=20	• The first principal component describes more than 70% of the motion data variance in thoracic and abdominal surfaces.
	Aoki et al., 2012 [26]	Volume respiratory waveform	Expiration gas analyzer, s=4	• p <0.001 • ρ >0.98
	Benetazzo et al., 2014 [28]	Respiratory rate	Spirometer, s=5	• p <0.001 • ρ =0.98
	Seppanen et al., 2015 [33]	Airflow waveforms	Spirometer, s=8	• $r^2 = 0.93$
	Heß et al.,2015 [35]	Abdominal and thoracic motion	Moving a high-precision platform with 10 micrometer accuracy, s=10	• abdominal region: $\rho = 0.74$±0.17 • Thoracic region: $\rho = 0.45$±0.23
	De Boer et al., 2010 [40]	Chest volume changes	Spirometer, s=40	• $r^2 = 0.91$ (volume) • $r^2 = 0.97$ (forced expiration)
	Yu et al., 2012 [41]	Tidal volume	Spirometer, s=1	• ρ =0.96
	Ostadabbas et al., 2014 [42]	• FVC • FEV1 • Airway resistance	Spirometer, s=5	• ρ =0.88
Prediction model using PDF	Alnowam et al., 2010 [27]	Respiratory motion	Marker-based tracking system, s=20	• *RMSD* = 0.78 mm
Optical Surface Imaging (OSI) system	Li et al., 2015 [43]	Tidal volume	Spirometer and CT imaging, s=3	• $r^2 = 0.99$ (CT imaging) • ρ =0.98 (spirometer)
Laser Doppler vibrometry (LDV)	Sirevaag et al., 2016 [46]	Respiratory rate and Heart rate	Comparison of 4 respiratory phases inspiration active, inspiration peak, expiration active and expiration peak, s=32	• ρ = 0.99 (correlation between mean values at each of the four respiration phases).

TABLE 1. *(Continued.)* **A comparative overview of the differences between previous methods in respiratory assessment.**

Method /device	Author name, year	Measured parameter	Validation method, validation dataset	Results with respect to each study's objective
3D surface reconstruction using RGB-D sensors	Sharp et al.,2017 [31]	Respiratory function testing • FVC • FEV1 • VC • IC	Spirometer, s=251	• FVC (r=0.999, p< 0.001) • FEV1(r=0.937, p< 0.001) • VC (r = 0.998, p < 0.001) • IC (r = 0.995, p < 0.001)
	Rehouma et al., 2018 [32]	• Respiratory rate • Tidal volume	Mechanical ventilator, s=1	• Respiratory rate: (RE=3.25%, RSD=9.87%) • Tidal volume: • (RE=9.17%, RSD=12.3%)
	Schaller et al., 2008 [39]	Respiratory signal	Respiratory gating System ANZAI belt (AZ733V, ANZAI Medical Co.), s=13	• ρ =0.88

OEP: optoelectronic plethysmography, ***s***: number of subjects, r^2: Coefficient of determination, ***d1***: discrepancy between OEP and Spirometry, ***d2***: discrepancy between *OEP* and pneumotachography, ***d3***: discrepancy between spirometry and pneumotachography, ρ: correlation coefficient, ***p***: no-correlation coefficient, ***PDF***: Probability Distribution Function, ***ToF***: Time-of-Flight, ***FVC***: Forced vital capacity, ***FEV1***: Forced expiratory volume in 1 second, ***VC***: relaxed vital capacity, ***IC***: inspiratory capacity, ***ROI***: Region of Interest, ***PCA***: Principal Component Analysis, ***CT***: computerized tomography, ***RE***: Relative Error, ***RSD***: Relative Standard Deviation.

diagnostic tool to observe the most active regions in the thoraco-abdominal region during breathing exercises on an indoor bicycle or in a treadmill workout. However, quantitative evaluation is not possible using this approach. Moreover, the system requires a complicated calibration process using five markers attached to the thoraco-abdominal region, which limits the clinical application of this technique.

Among the ToF-based approaches, Penne *et al.* [37] computed the breathing signal using a single ToF camera. Their approach is based on computing the best-fitting planes for two ROIs corresponding to the abdominal and thoracic regions. Respiration signal estimations were derived by calculating the displacement of each plane to a plane representing the patient's couch. To validate their approach, the authors compared their results to those obtained from an ANZAI belt (AZ- 733V, ANZAI Medical Co.) for chest and abdomen regions. Good correlation results were reported for both thoracic and abdominal regions. Falie et al. recorded a patient's thoracic and abdominal movements during sleep using an SR3000 model ToF camera [38]. By dividing the chest wall into 12 zones, they analyzed the motion in each zone separately to detect any irregular breathing or respiratory arrest during sleep. Shaller et al. used the SR3000 ToF camera to estimate a real-time multidimensional respiratory signal from a 3D surface reconstruction of a patient's chest wall without using any markers [39]. They reported that it is feasible to acquire a 3D model in real time using a single camera, and to compute the thoracic and abdominal breathing motions simultaneously. They also mentioned that their method allows splitting the chest wall into many regions and estimating their respective breathing patterns. To validate their technique, the authors acquired thoracic and abdominal breathing patterns using an external gating system, the ANZAI belt, as a reference method. Their results showed a strong correlation between the patterns of the two techniques.

Despite the significant progress made in chest wall assessment, there is still a need for methods to visualize and quantify chest wall motion for a more concrete and precise characterization of respiratory diseases. Indeed, the proposed non-contact methods include breathing waveform estimation, motion data variance in the respiration region and physiological parameters estimation, but they do not include quantitative assessment of the chest wall motion and deformation visualization, without having to use markers attached to the chest wall. Currently, there are no quantitative reference values for chest wall distortion allowing to estimate the severity of a respiratory failure.

In this study, the classification of TAA is a modification of a previous disease severity score (DSS), used by Gern *et al.* [47], Wishaupt *et al.* [48]. Chest wall deformities are subdivided into mild and severe. These TAA modes are compared to a reference mode, which we have called the normal mode. Indeed, the normal mode is defined by the coordinated expansion of the thoraco-abdominal compartments. The two compartments are in phase. When considering the breathing pattern, this mode is similar to normal physiological human breathing and is our gold standard. TAA in both mild and severe forms is shown by an uncoupling of the ribcage-abdominal motion that may result in a decrease in tidal volume (Vt), a decrease in alveolar minute ventilation (MV) and thus ventilatory failure [49]. More specifically, the mild TAA mode is defined by a non-parallel expansion of the rib cage (RC) and abdominal (AB) compartments relative to the normal mode. This mode is characterized by opposing movements with small amplitude changes and a potential slight phase shift between the thorax and abdomen regions.

This asynchrony in movement between RC and AB indicates a certain level of diaphragm weakness [3]. This TAA mode is difficult to observe with the naked eye, and its detection is highly correlated to the clinician's expertise. However, this mode is characterized by a slightly increased work of breathing (WOB). Severe TAA mode is defined by a non-parallel expansion of the rib cage (RC) and abdomen (AB) compartments. This mode is characterized by opposing movement with large amplitude changes and a potential slight phase shift between the thoracic and abdominal regions. The severe TAA mode movements indicate a high level of diaphragm fatigue that may lead to respiratory failure [3]. These retractions are clearly visible to the naked eye through physical examination by caregivers, and are frequently seen in critically ill children with respiratory disorders [3], [50]. The irregular TAA mode is a random expansion order of the rib cage and abdomen of the three thoraco-abdominal deformities described above.

We have developed a non-contact system to identify and quantify the motion of the thoraco-abdominal region patterns in patients with TAA. The system uses a single RGB-D camera to estimate a dense and instantaneous 3D motion field corresponding to the motion of the surface due to breathing. To estimate a 3D dense motion field, the system takes advantage of the RGB-D camera's features by using both acquired color and depth data simultaneously, and by exploiting its good spatial and temporal resolution. Our approach is thus based on considering these three important factors: spatial resolution, temporal resolution and the use of multiple streams (color and depth data) to collect detailed information about breathing patterns. The main objective is to verify that the new non-contact system is efficient and reliable for identifying and quantifying TAA.

III. MATERIALS AND METHODS

A. CAMERA SYSTEM AND SENSING PROPERTIES

An RGB-D sensor, also called range sensor, is a camera device equipped with a class1 laser operating at near infrared (IR) wavelengths (∼830nm). A variety of 3D sensors, exploiting two main categories of working principles, have been introduced into the market. The first category is based on the structured light (SL) triangulation technique. The system utilizes an IR laser projector that constantly projects a refraction pattern on the scene, an infrared camera that observes this pattern, and a color camera. As the projected pattern is known, it is possible to compute the disparity using computer vision techniques. Algorithms, such as image rectification and block matching, are implemented in a System-on-a-Chip (SoC) unit and processed internally in the device. These vision algorithms estimate the distance for each image pixel [51]. The second category is based on the Time-of-flight (ToF) technique. The device incorporates almost the same components as triangulation-based devices with two electronic modules (IR and RGB). The sensor uses an infrared flash module that determines the distance to objects by measuring the round-trip travel time of an amplitude-modulated light from the source to the target and back to the camera at each pixel [52], [53].

Three simultaneous streams can be captured using an RGB-D sensor: Color (RGB), Depth (D) and Infrared Radiation (IR). Multiple RGB-D cameras have been released by Intel and Microsoft over the last few years. However, those devices presently work with a borderline level of acceptance of their depth resolution. Most of the new RGB-D cameras provide registered RGB and depth images at a fairly high frame rate (30 Hz), which presents an advantageous setting for the implementation of real-time computer vision algorithms. Many studies have investigated the performance of RGB-D cameras, such as the Kinect v1 structured-light sensor [54], [55], the Kinect v2 time-of-flight sensor [52], [56], [57] and Asus Xtion structured-light camera [34]–[36]. The Kinect sensors (v1 and v2) have been widely used in many studies due their promising properties. However, an electronic box consisting of a power supply and a USB extension is required to connect the Kinect sensor to a computer, making for a complex and demanding installation. Unlike Kinect cameras, the Asus Xtion is very user friendly, presents a small size and does not require complex installations to be used with a laptop. There is no need for an alimentation cable or a specific USB adapter. Moreover, the Asus Xtion sensor can run well on any computer system, unlike the Kinect sensor which requires a USB 3.0 port to transfer the data between the camera and the computer. Furthermore, the images in the two streams are time-stamped by a common clock. The shutters are not in sync, but the time stamps can be used to match color images to the closest depth images, a significant advantage of the Asus Xtion Pro Live Motion over the Kinect camera. The main advantage of using the Kinect is the ease of skeleton detection using the skeleton joints provided in the Kinect SDK (20 joints for the Kinect v1 and 25 joints for the kinectv2), which is not needed in this work. The Asus Xtion Pro Live Motion Sensing Camera therefore has many advantages, and is the camera used in this work.

A schematic representation of our RGB-D imaging system is given in Figure 1. Figure 1.a shows the Asus Xtion Pro Live commercial model, and a partially disassembled sensor (in the bottom). Figure 1.b presents a schematic diagram of the technology employed by the Asus Xtion Live camera. Figures 1.c and 1.d illustrate a sample frame (color and depth) of a ball and an office cabinet, respectively, observed with the RGB-D sensor. The color and depth images have a same resolution of 640 × 480 pixels. The depth frame is a gray-scale format image whose pixels values indicate the distance between objects in the scene and the sensor. As shown in Figure 1-d, the intensity of objects (ball, office cabinet and the wall) varies, depending on their proximity to the camera.

B. MOTION ESTIMATION

Optical flow is the computer vision algorithm most widely used to estimate a dense motion. However, optical flow formulation only allows motion estimation in 2D and not in 3D.

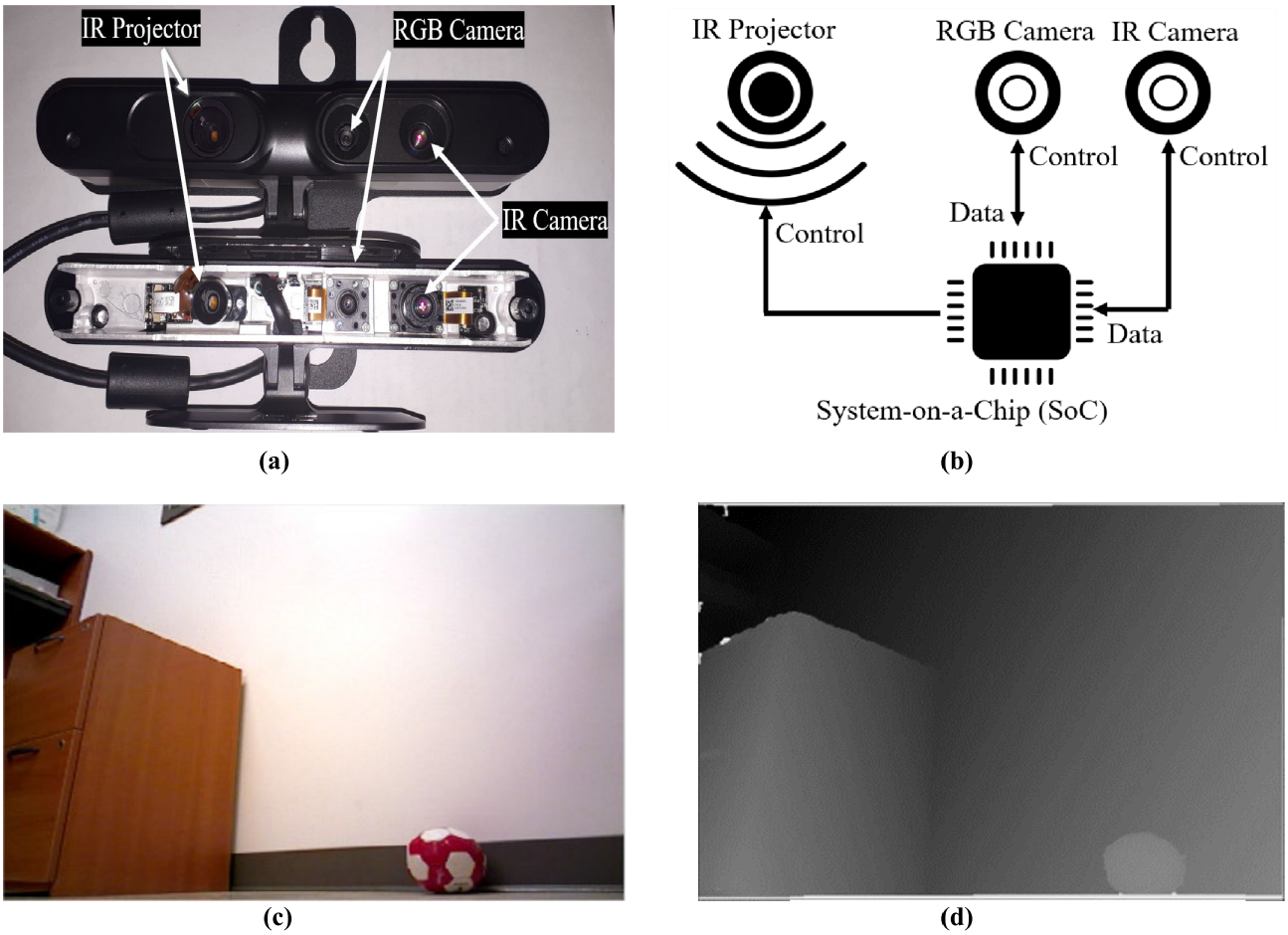

FIGURE 1. RGB-D camera description: (a) The used Structured-Light RGB-D sensor (Asus Xtion Pro Live) and the partially disassembled sensor (bottom), (b) A schematic diagram of the Asus Xtion Live camera structure, (c) The acquired RGB image, (d) The acquired depth image.

Estimating the 3D motion requires more prior information than optical flow. The RGB-D camera provides depth data that allows for 3D motion estimation. The RGB-D camera thus allows the 3D motion of points in the scene to be estimated effectively using both color and depth frames simultaneously.

The aim is to calculate the dense 3D motion field of a scene between two instants of time, t and $t+1$, using color and depth images recorded simultaneously by the RGB-D sensor.

The motion estimation approach first assumes that color and depth images are presenting the same size. This is provided straightforwardly by using the Asus Xtion RGB-D sensor.

Let $M : (\Omega \in \mathbb{R}^2) \rightarrow \mathbb{R}^3$ denote the motion field, where Ω is the image domain. M is expressed in terms of the optical flow u, v and the range flow w. For any pixel with a nonzero depth value, the bijective relationship $\Gamma : \mathbb{R}^3 \longrightarrow \mathbb{R}^3$ between M and $\boldsymbol{V} = (u, v, w)^T$ is given by (1):

$$\boldsymbol{M} = \Gamma(\boldsymbol{V}) = \begin{pmatrix} \frac{Z}{f_x} & 0 & \frac{X}{Z} \\ 0 & \frac{Z}{f_y} & \frac{Y}{Z} \\ 0 & 0 & 1 \end{pmatrix} \begin{pmatrix} u \\ v \\ w \end{pmatrix} \tag{1}$$

Equation (1) can be deduced directly from the well-known "pin-hole model", where f_x and f_y are the focal length values and X, Y, Z the spatial coordinates of the observed point.Following the differential model provided by Horn and Schunk [58], who provided the first formulation of optical flow, the problem of motion estimation can be formulated as a minimization problem of a certain energy functional. From a general perspective, there are three main points in an optical flow algorithm: 1) the formulation of the energy to be minimized; 2) the discretization scheme; and 3) the solver used to minimize the energy [59]. Hence, the motion field is computed from the resolution of (2):

$$min_{\boldsymbol{V}} \{E_D(\boldsymbol{V}) + E_R(\boldsymbol{V})\} \tag{2}$$

In (2), the sum of the data and the regularization terms is minimized over $\boldsymbol{V}$. The first term $E_D(\boldsymbol{V})$ represents the data term, including both color and depth data, while the second term $E_R(\boldsymbol{V})$ is the regularization term used to smooth the flow field and to constrain the solution space. The resolution of the minimization problem described in (2), can be found in [60], along with the implementation details.

C. MOTION SEGMENTATION

The goal is to regroup motion vectors that have almost the same moving direction (either towards or away from the camera) in order to differentiate between the main surface deformation schemes. These deformations result from air movement into and out of the lungs, which depends upon changes in pressure and volume in the thoracic cavity. Since air is always flowing from an area of high pressure to an area of low pressure, changing the pressure inside the lungs, using the intercostal muscles and the diaphragm determines the direction of airflow and the surface deformation scheme.

There are roughly two possible deformations of the 3D surface, either approaching or moving away from the camera. Accordingly, we mainly subdivide the calculated 3D vector motion fields into a set of two groups, corresponding to inward and outward movements. We used the Euclidian distance, as shown in (3), to assess the similarity between depth motion map vectors' ($DMMV$) directions. Let $\mathcal{M}$ be the total motion field on the surface S_1. Each 3D vector motion field $\boldsymbol{V}$ $(x_{i+1} - x_i, y_{i+1} - y_i, z_{i+1} - z_i) \in \mathcal{M}$ is either moving towards ($DMMV_{out}$) or away from the camera ($DMMV_{in}$). This is represented by (4) and (5).

$$d_i^2 = x_i^2 + y_i^2 + z_i^2 \tag{3}$$

$$DMMV_{in} = \left\{ \boldsymbol{V_i} \in \mathcal{M} \backslash d^{t+1} > d^t, i \epsilon 1..N \right\} \tag{4}$$

$$DMMV_{out} = \left\{ \boldsymbol{V_i} \in \mathcal{M} \backslash d^{t+1} < d^t, i \epsilon 1..N \right\} \tag{5}$$

where i indicates a 3D point, (x, y, z) are the spatial coordinates of a 3D point i, V is the motion field of a 3D point i, $\mathcal{M}$ is the total motion field, N is the number of 3D points over the surface S_t and $\boldsymbol{d^t}$ is the Euclidian distance from the origin of the coordinate system at frame t. The following mathematical symbol "/" indicates a "such as" condition.

In Figure 2, the Euclidian distance d^t is calculated for all motion vectors at their origins and compared to the distance d^{t+1} at frame t+1. This comparaison allows the clustering of the motion vector fields into outward and inward movements. For example, the comparison of the Euclidian distances in V_1, V_2 and V_3 yields to adding V_1 and V_2 to the $\boldsymbol{DMMV_{out}}$ cluster and adding V_3 to the $\boldsymbol{DMMV_{in}}$ cluster.

Consider there are M point clouds on each surface and N surfaces. For each surface $S^j, j \in \{1..N\}$, two subsurfaces S^j_{in} and S^j_{out}, corresponding to the inward and outward movements of S^j, respectively, are extracted as shown in (6) and (7). For example, S^1_{in} is the subsurface of S^1 moving inwards. The rest of the surface is set to zero. Only the surface's points moving inwards are saved. Likewise, S^1_{out} is the subsurface of S^1 moving outwards.

$$S^j_{in} = \left\{ p_i\,(x_i, y_i, z_i) \in S^j / V_i \in DMMV_{in} \right\},\ j \in \{1..N\} \tag{6}$$

$$S^j_{out} = \left\{ p_i\,(x_i,\ y_i, z_i) \in S^j / V_i \in DMMV_{out} \right\},\ j \in \{1..N\} \tag{7}$$

IV. EXPERIMENTAL SETUP

The experiments were performed on a baby mannequin (SimBaby, Laerdal ®) designed for medical pediatric simulation with specific anatomical and physiological characteristics. This mannequin was used to simulate the retractions. The simulations were conducted in the simulation center at Sainte-Justine Hospital in Montreal, which presents the same conditions as a pediatric intensive care unit room.

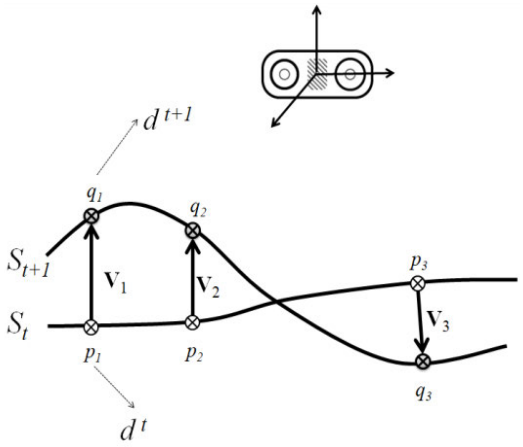

FIGURE 2. Motion extraction technique based on comparing distances from the RGB-D sensor, whose center is the origin of the coordinate system. The surface S_t is represented by M 3D point clouds $p_j, j \in \{1..M\}$ at frame t, whose projection is on the surface S_{t+1} at frame t+1 are $q_j, j \in \{1..M\}$. For every motion vector $V_i \in \mathcal{M}$, the Euclidian distance in the 3D space between the vector points and the camera's center are calculated and compared. This comparison allows to determine the motion direction. For V_1, $d^{t+1} < d^t$, V_1 is moving towards the camera ($DMMV_{out}$) which correspond to an outward movement. For V_3, $d^{t+1} > d^t$ and V_3 is moving away from the camera ($DMMV_{in}$) which corresponds to an inward movement.

The experimental environment also includes an Asus Xtion RGB-D sensor placed one meter over the mannequin and two VL53L0X laser-ranging sensors. The VL53L0X sensor is a fully integrated sensing system with an embedded 940 nm infrared VCSEL (vertical-cavity surface-emitting laser) array. VCSELs are characterized by their narrow and stable emissions when compared to the conventional wide spectrum of LEDs (light-emitting diodes). The VL53L0X distance sensor system uses Time-of-Flight (ToF) technology to accurately measure the distance to a target object. The sensor is independent of the target's color or reflectivity and can report distances of up to 2 m with 1 mm resolution [61], [62]. A 940 nm laser detector card was used to detect the invisible laser beam on the mannequin's thoraco-abdominal surfaces.

Four modes were recorded: normal breathing mode without any TAA, mild TAA, severe TAA and irregular mode. In normal conditions, the thorax and abdomen inflate simultaneously during inspiration and deflate simultaneously during expiration. In TAA, the thorax deflates while the abdomen inflates, reflecting the high level of negative intra-thoracic pressure during inspiration. During expiration, the thorax inflates while the abdomen deflates. In the mild mode, the thoracic deflation is less intense compared to the severe mode, and thus the distance between thorax and abdomen

will be lower. In irregular mode, the SimBaby will create random cycles with either normal or mild TAA or severe TAA. The mode and the respiratory rate are triggered by a board computer linked to the mannequin. A fixed respiratory rate of 35 breaths /minute (BPM) was selected for the simulations.

Data was recorded over one minute for each mode in this order: normal, mild TAA, severe TAA and irregular mode.

Two sets of experiments were performed. In the first set, the depth variations of the retraction zone were simultaneously recorded using the RGB-D camera and the VL53L0X high-precision laser. The laser was used to validate the retraction distances calculated by the proposed method. The camera was positioned one meter above the thoraco-abdominal zone and was pointing downwards. As shown in Figure 3, the camera was positioned in a vertical or slightly angled position so that variations along the X- and Y-axes are insignificant when tracking the position of a 3D point in the camera coordinate frame. The lasers were wrapped around the camera. The first laser calculates the distance variation in the thoracic region, and the second laser calculates the distance variation in the abdominal area. In the second set of experiments, the impact of the camera positioning on the algorithm performance was investigated. Different camera positions were compared to the vertical position. The retraction zone's depth was calculated from different viewing angles to evaluate the accuracy of the proposed method.

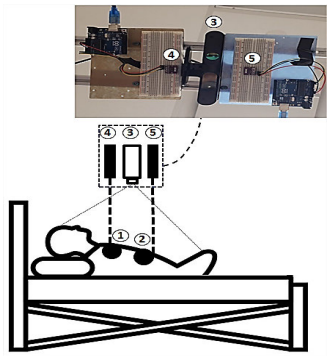

FIGURE 3. First round of experiments setup: (1) ROI 1: Thoracic area; (2) ROI 2: Abdominal area; (3) RGB-D camera pointing to the thoraco-abdominal area; (4) Laser-ranging sensor pointing to a point in ROI1; and (5) Laser-ranging sensor pointing to a point in ROI2.

V. RESULTS AND DISCUSSION

A. VISUALISATION

The thoraco-abdominal zone was extracted as described in section IV. This zone includes the areas of interest, whose motion are given by a 3D dense point cloud describing the patient's breathing. Different data types are shown in Figure 4. The raw data is composed of RGB and depth images. The point cloud (X, Y, Z) is derived from depth images, while the colored point cloud is calculated from both depth and RGB data. Figure 4-f shows the calculated scene-flow using the method in [60], where the blue points are the initial positions of 3D points (at frame t) and the red points are the final positions (at frame t+1).

The inspiration movement corresponds to a 3D motion towards the camera, while expiration is a 3D motion in the opposite direction. In the case of TAA, the two motions occur almost simultaneously in two different regions of the thoraco-abdominal zone. As shown in Figure 6, the chest and abdomen are moving opposite to each other's directions. These movements are detected by our extraction technique. Using our method for motion extraction presented in sub-section III.C, it is possible to extract two sub-regions according to the inwards or outwards movement of the point cloud. The 3D point clusters moving forwards are depicted in red, while the 3D point clusters moving backwards are colored in blue. As shown in Figure 6, the breathing motion has been simulated using the phantom. Three categories of movements corresponding to the inspiration, expiration and TAA, are clearly visible. During normal inspiration, the lungs are inflated by the expansion and contraction movements of the diaphragm and the ribs that give the thorax its shape. Figures 6-a, 6-b and 6-c represent inspiration motion. Most of the 3D points are colored in red due to the forward movement of both chest and abdomen.

Expiration is a passive movement in which the lungs act like a deflating balloon. Figures 6-d, 6-e and 6-f are showing the expiration motion. Most of the 3D points are colored in blue due to the inward movement of the chest and the abdomen. Figures 6-g, 6-h, 6-i, 6-j, 6-k and 6-l represent the paradoxical motion. Since the chest moves in the opposite direction of the abdomen, both red and blue colors can be seen and are more equitably distributed between 3D point clouds. The movements of the rib cage are paradoxical relative to those of the abdomen and to airflow. Figures 6-g, 6-h and 6-i represent the inspiration in TAA. The thorax is deflating and thus the region is represented with a blue point cloud, while the abdomen point cloud is represented in red. This means that the rib cage is moving inward while the abdomen is moving forwards. Figures 6-j, 6-k and 6-l represent expiration in TAA. The chest region is represented with a red point cloud while the abdomen point cloud is shown in blue. In Figures 6-c, 6-f, 6-i, and 6-l, we apply a translation between the two clusters moving forwards and backwards in order to visualize them clearly in two different planes.

B. VALIDATION METRICS

1) CLOUD-TO-SENSOR DISTANCE

We consider the set of surfaces $S^j, j \in \{1..N\}$ and define $daverage^j_{in}$ and $daverage^j_{out}$ as the average distances from the camera to the inward S^j_{in} and outward S^j_{out}, moving sub-surfaces, respectively. The distance between a 3D point $p_i\,(x_i, y_i, z_i)$ and the sensor is the Euclidian distance, given in (3). The cloud-to-sensor distance is defined in this work as the average distance from the camera to the cloud over all 3D points in the cloud. The cloud-to-sensor distance is calculated from the camera to the two sub-surfaces S^j_{in} and S^j_{out} in order to obtain the average motion signal for both

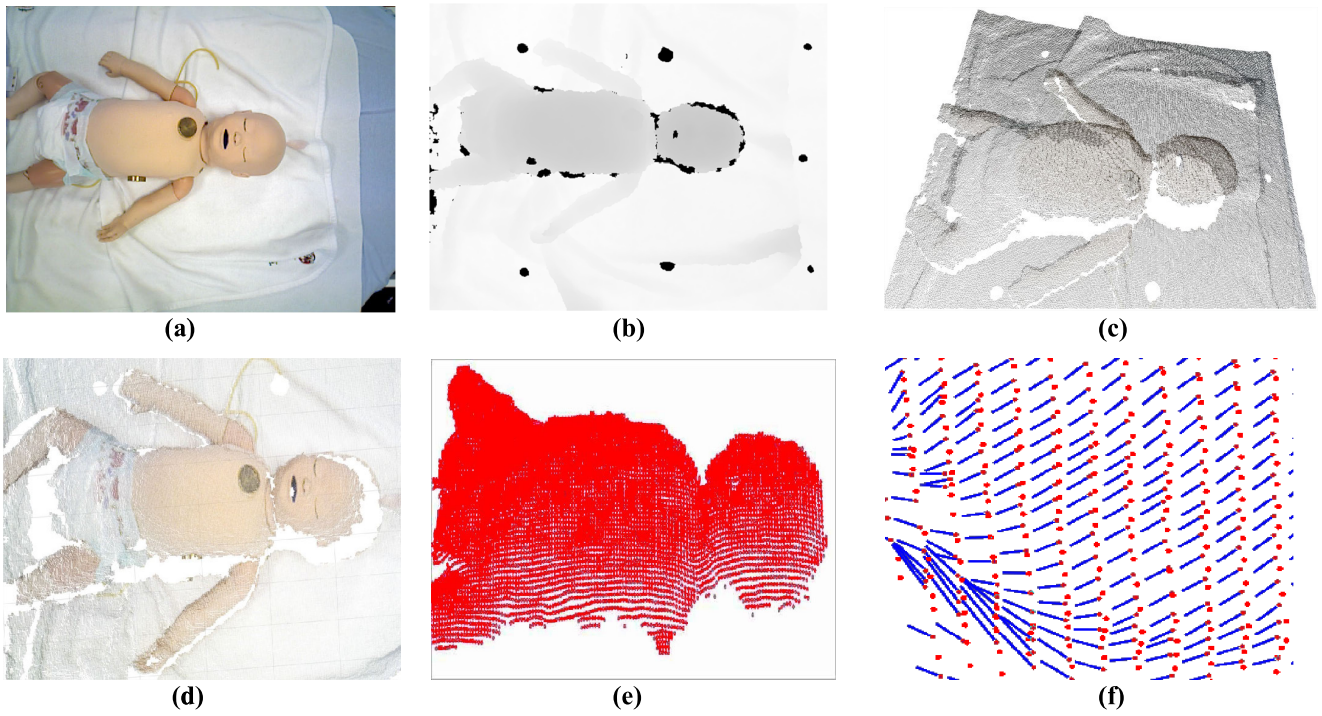

FIGURE 4. Illustrations of mannequin acquired and treated data: (a) RGB image, (b) Depth image, (c) Point cloud (X, Y, Z), (d) Colorized point cloud (X, Y, Z, R, G, B), (e) Segmented ROI, (f) Calculated scene flow.

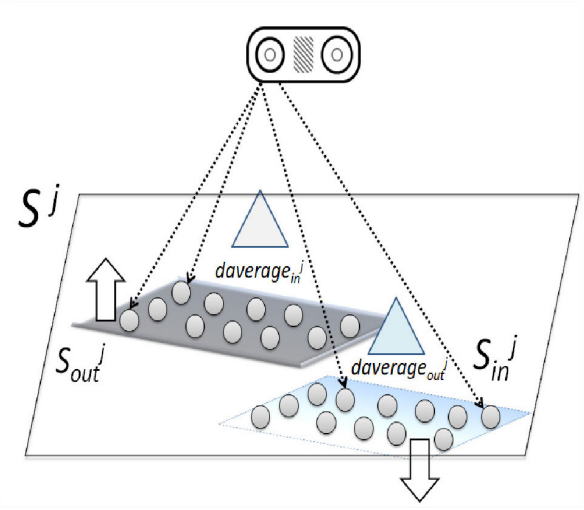

FIGURE 5. Cloud to sensor distance estimation at the frame j.

retraction regions as well as to estimate the retraction distance on the two regions.

As shown in Figure 5, the distances $daverage_{in}^j$ and $daverage_{out}^j$ are calculated for each frame $j \in \{1..N\}$ between the sensor and the two extracted surfaces S_{in}^j and S_{out}^j, allowing the estimation of chest and abdominal motions.

2) CLOUD-TO-CLOUD DISTANCE

Tracking 3D points in point clouds data during breathing is complicated in a very acutely-angled position. Displacement variations along the X- and Y- camera axes are more important than in the case when we place the camera vertically above the thoraco-abdominal zone. For this reason, we use a method that takes into consideration displacements along the X- and Y- camera axes.

We consider S^j and S^{j+1} to be the thoraco-abdominal surfaces at two consecutives frames, as indicated in Figure 7. Point clouds of surface S^{j+1} are regarded as "target" points $p^{S_{j+1}} = \left(p_x^{S_{j+1}}, p_y^{S_{j+1}}, p_z^{S_{j+1}}\right)$, whereas the point clouds of the surface S^1 are the original points $p^{S_j} = \left(p_x^{S_j}, p_y^{S_j}, p_z^{S_j}\right)$. The distance between 3D points is calculated using the Euclidian distance in the space $\mathbb{R}^3$. The aim is to find the corresponding 3D points before and after the surface displacement from S^j to S^{j+1}. Consider that we have M source points in cloud $p_i^{S_j}$ on the surface S_j. Points $p_i^{S_j}, i\epsilon\{1..M\}$ from S^j are projected on S^{j+1} using the normal vector at each source point, as shown in Figure 7. The projected points are noted as $p_i'^{Sj+1}, i\epsilon\{1..M\}$. To find a corresponding destination point in S^{j+1}, the nearest neighbor is selected in $p_i^{S_{j+1}}, i\epsilon\{1..M\}$. The displacement distance is then computed for each pair $(p_i^{S_j}, p_i^{S_{j+1}})$.

In Figure 8, the source point $p_1^{S_{j+1}}$ on the surface S^j (cloud in frame j) is projected on the surface S^{j+1}(cloud in frame j+1) using the normal vector in $p_1^{S_j}$. As can be seen, the nearest neighbors of the projected point $p_1'^{Sj+1}$ are $p_1^{S_{j+1}}, p_2^{S_{j+1}}, p_3^{S_{j+1}}$ and $p_4^{S_{j+1}}$. Since $p_1^{S_{j+1}}$ is the closest point to the projection $p_1'^{Sj+1}$, it is selected as the corresponding point of $p_1^{S_j}$. Finally, the displacement distance

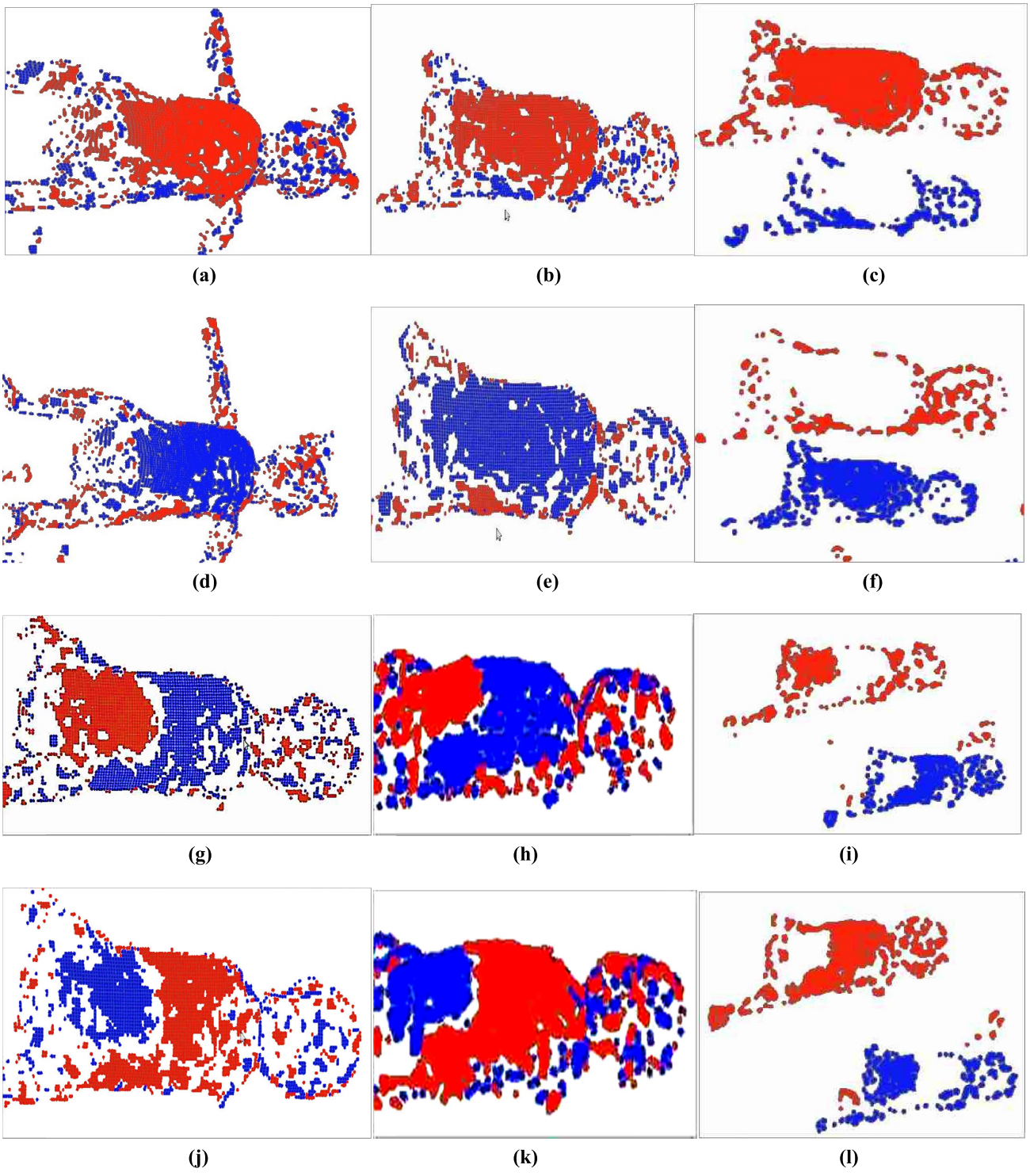

FIGURE 6. Regions extraction obtained for point cloud frames in the tested sequences: (a), (b) and (c) represent normal inspiration, (d), (e) and (f) represent normal expiration, (g), (h), (i), (j), (k) and (l) represent TAA. Clusters segmented as forward motion are represented in red and clusters segmented as backward motion are colored in blue. In (c), (f), (i) and (l), we apply a translation between the extracted regions in order to visualize them more clearly and distinctly.

$d_1^{S_jS_{j+1}}$ is computed for the pair $\left(p_1^{S_j}, p_1^{S_{j+1}}\right)$ by calculating $\left\|p_1^{S_{j+1}} - p_1^{S_{j+1}}\right\|_2$. By iterarting the procedure of finding corresponding 3D points between consecutives frames and calculating the distance between initial points and their projections, we get a vector of distances $d_i = \left(d_i^{S_1S_2}, d_i^{S_2S_3}, d_i^{S_3S_4}.., d_i^{S_{N-1}S_N}\right)$, i $\in$ {1..N}. Finally, the Δd_i distance is calculated by summing the distances between the different projections of the initial 3D point (sum of d_i

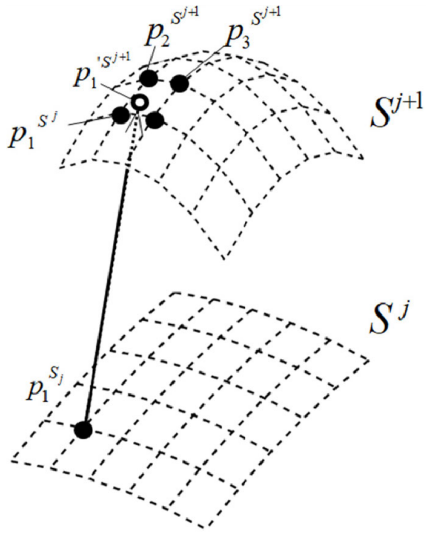

FIGURE 7. Finding corresponding pairs of 3D points between consecutives frames.

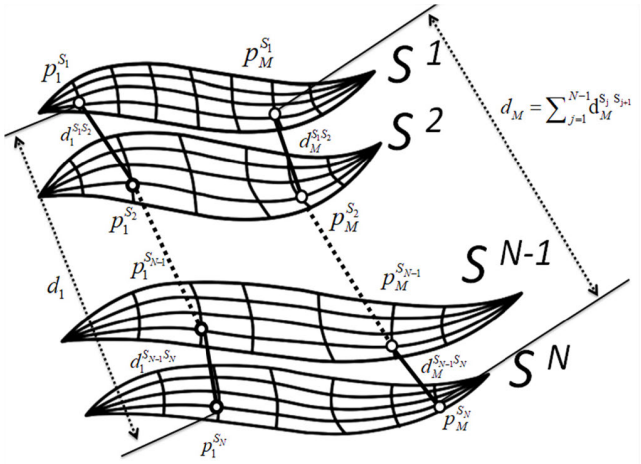

FIGURE 8. Computing of cloud-to-cloud maximal displacement between surfaces.

vector components). Δd is the maximum of Δd_i over M point clouds (i $\in$ {1..M}).

To summarize, consider a cloud of M source 3D points $p_i^{S_1}$, i $\in$ {1..M} and N surfaces (S_1, S_2, ..,S_N). The proposed algorithm has two main steps. First, correspondences between 3D points and their projections on the consecutive surface are found, and then the distances between each 3D point and its projections on the N surfaces are calculated. Specifically, this second step is computing the distances $d_i^{S_j S_{j+1}}$, i $\in$ {1..M} and j $\in$ {1..N} between the clouds for each 3D point on the surface S_j and its projection on the surface S_{j+1}. The maximal displacement between S_1 and S_N is given by (8).

$$\Delta d = \max_{i\in\{1..M\}} \left(\sum_{j=1}^{N-1} d_i^{S_j S_{j+1}} \right) \tag{8}$$

Note that cloud-to-cloud maximal displacement is calculated over the two sub-surfaces S_{in}^j and S_{out}^j.This technique obtains the direction of the surface motion, estimates the distance of the different 3D point paths after displacement and calculates the maximal path.

C. COMPARISON BETWEEN LASER AND CAMERA IN THE VERTICAL POSITION

In the first experiment, the camera and the two lasers are placed vertically to the thoraco-abdominal zone, which makes variations negligible along the X- and Y-axes.

Experiments were performed for normal conditions and for three TAA modes: mild, severe and irregular. The 3D point clouds moving in the same direction were grouped into the same cluster by using our technique presented in sub-section III.C. Indeed, the motion extraction technique determines the number of sub-surfaces. In normal respiration, only one region corresponding to inspiration or expiration is extracted. In TAA, two sub-regions are extracted. These sub-regions are corresponding to the opposite motion of the thorax and the abdomen. The average distance is calculated relative to each sub-region of 3D point clouds, using the technique described in paragraph V.B.

The results obtained from the setup in Figure 3 are illustrated in Figure 9, which shows the results of the four experiments corresponding to normal respiration, mild TAA, severe TAA, and irregular modes. These results show that both techniques (laser and video) are correlated and reliable whatever the conditions. Thoracic and abdominal movements are in-phase with synchronous movements of the two components in normal mode, but in TAA modes, the signals produce a characteristic pattern of paradoxical motion with the two components working in opposition. The maximum-to-minimum amplitude between thoracic and abdominal signals represents the retraction difference between the two regions of interest. In the irregular mode, thorax and abdomen are in phase during a normal cycle and in opposition during a TAA cycle, in random order. The intensity of opposition varies according to the severity of the TAA.

As shown in Table 2, the retraction distance is calculated by averaging the maximum-to-minimum amplitude between the thoracic and abdominal respiration signals during one minute of recording. The respiratory rate can be calculated by simply counting the number of peaks in a minute. However,

TABLE 2. Retraction distance estimation using laser-ranging sensors and the proposed method. The laser and the camera are placed in vertical positions. Δd_{laser} is the retraction distance ± the standard deviation of the result over one minute as calculated using the laser, while Δd_{camera} is the retraction distance ± the standard deviation of the result over one minute as calculated using the proposed method. The relationship and the comparison between the proposed and the reference methods are illustrated through the correlation coefficient ρ and the root mean square deviation (RMSD).

Experiment number	Mode	Δd_{laser} (cm)	Δd_{camera} (cm)	ρ	*RMSD* (mm)
1	Normal	0,27±0,11	0,23±0,13	0,994	1,78
2	Mild	1,98±0,18	1,95 ±0,24	0,989	2,83
3	Severe	3,52±0,23	3,64±0,41	0,992	2,23
4	Irregular	2,82±063	2,77±0,11	0,986	2,34

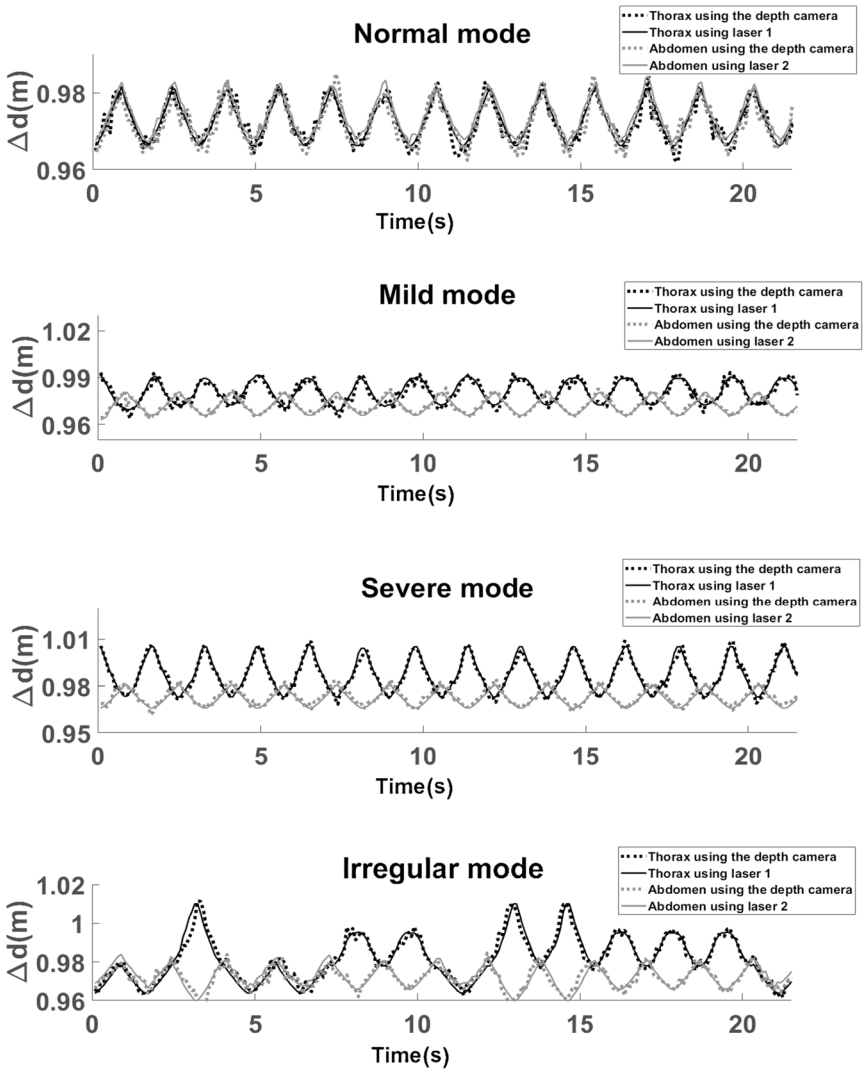

FIGURE 9. Our method's curves for estimating abdomen (ROI2) and thorax (ROI3) depths are plotted in dotted black lines and dotted gray lines, respectively. Their corresponding depth curves calculated using the laser-based sensors are indicated, in plain black and plain gray lines, respectively. The modes are: normal respiration, mild TAA, severe TAA and irregular mode.

to improve the accuracy of our method, we use (9) where RR, expressed as the number of respirations per minute, is the respiratory rate, and N is the number of peaks during the observation time ΔT (in seconds).

$$RR = \frac{N * 60}{\Delta T} \tag{9}$$

The retraction distance is 1.95 ±2.4mm in mild mode, 3.64 ±4.1mm in severe mode, and 2.77±1.1mm in irregular mode. The results show a very good correlation between the two methods for the four modes (>0.985) and small RMSDs of 1.78 in normal mode, 2.83 mm in mild mode, 2.23 mm in severe mode, and 2.34 in irregular mode. In the normal mode, thoracic and abdominal signals are in-phase and hence, Δd_{laser} and Δd_{camera} are calculted by considering the maximum-to-maximum amplitude between the proposed method (RGB-D camera) and the reference signal (laser). It is clear that the amplitude of the abdominal region signal is lower than that at the thorax region in both severe and mild modes, and slightly higher in the normal mode. The respiratory rate is 34.75 ±0.4BPM in normal mode, 35.19 ± 0.2BPM in mild mode, 34.8 ±0.35BPM mm in severe mode and 34.66±0.5BPM in the irregular mode.

D. CAMERA POSITION VALIDATION

In the second set of experiments, five cameras were placed in different positions around the mannequin, as shown in Figure 10. The cameras were positioned in the (a) bed top left, (b) bed top right, (c) bed bottom left, and (d) bed bottom right. Each camera was oriented to the mannequin's thoraco-abdominal zone. In each experiment, the retraction distances were calculated for each position, and then compared to those

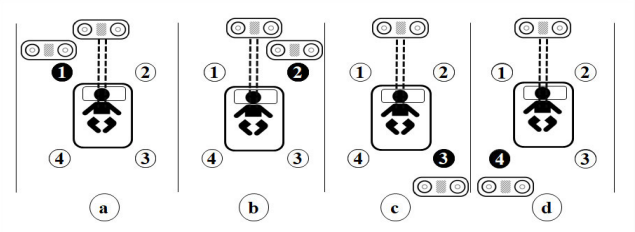

FIGURE 10. Second set of experiments setup and cameras positioning. The cameras are placed in the (a) bed top left, (b) bed top right, (c) bed bottom right and (d) bed bottom left. The reference camera sensor is always placed in a vertical position to the thoraco-abdominal area under the same conditions of those of the first set of experiments (see Figure 2).

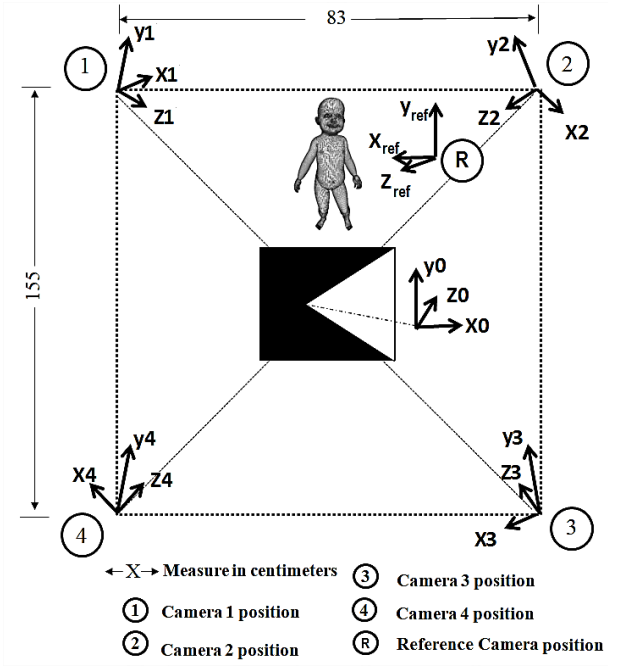

FIGURE 11. Estimating camera position using Procrustes alignment method.

calculated by the sensor placed in a vertical position. The experimental setup shown in Figures 10 and 11 is designed to evaluate the impact of changing the position around the bed on the system's accuracy. Considering the limited space in a Pediatric Intensive Care Unit (PICU), the camera can be placed on one of the four legs of the bed. It should be noted, however, that the top of the bed is often occupied by medical staff and other medical devices and thus, is not always accessible. Therefore, the two preferable locations to place the cameras are positions 3 and 4 (Figure 10), corresponding to the bottom of the bed. Nevertheless, the ideal operating position of the RGB-D camera is the vertical position. To investigate the impact of changing the position on the system's accuracy, the four bed positions (top left, top right, bottom left, bottom right) were tested and their results compared.

The experiments produced highly accurate results and showed significant agreement between the proposed method and the method using laser-ranging sensors when the camera is placed in a vertical position. However, placing the camera in a vertical position above the patient may be problematic when deploying the system in the pediatric intensive care environment. Any occupied space should not cause care interruptions or present a potential risk for patient safety. Moreover, caregivers need to provide the appropriate services with sufficiently free space around the patient. According to doctors, bed bottom positions are usually the most appropriate to place our camera. This sub-section evaluates the system performance when the camera is placed in four positions around the bed, at the bed top (camera #1 and #2) and bottom positions (camera #3 and #4).

The results obtained from the setup in Figures 10 and 11 are illustrated in Tables 3 and 4. Table 3 shows the results of experiments corresponding to the different cameras positions using the camera-to-cloud metric, whereas Table 4 shows the results of the same experiments and data using the cloud-to-cloud distance metric. In Table 3, the RMSD and correlation values are calculated for different modes between the new position (cameras #1, #2, #3 and #4) and the reference position (the camera in the vertical position). Next, the average RMSD and the correlation values are calculated for all modes together. The results show average RMSD values of 2.48mm for camera #1, 2.19mm for camera #2, 5.04mm for camera #3 and 5.84mm for camera #4. The correlation coefficients also reveal a high correlation between the reference measures and the quantitative data sets' measures corresponding to the different camera bed positions. Indeed, ρ is very high (> 0.98) for both bed head positions (cameras #1 and #2) and relatively high (>0.9) for the bottom bed positions (cameras #3 and #4). The proposed method's measures corresponding to the head positions are also highly correlated with the reference data (camera in the vertical position). Likewise, the small RMSD value indicates that the system performs very well for both bed head positions. However, RMSD values are slightly higher for bed bottom positions (5.04mm for camera #3 and 5.84mm for camera #4).

The cloud-to-cloud distance was also used to confirm the obtained results. The aim is to study the precision of the proposed 3D imaging system when changing the camera position around the patient's bed. The results show an average RMSD value of 2.55mm for camera #1, 2.42mm for camera #2, 5.99mm for camera #3 and 5.33mm for camera #4. The correlation coefficients reveal a very high correlation (> 0.99) for both bed head positions (cameras #1 and #2) and a high correlation (>0.95) for the bottom bed positions (cameras #3 and #4). Furthermore, the RMSD is small (less than 3mm) for both bed head positions, yielding very good accuracy, and slightly higher for bed bottom positions (5.99mm for camera #3 and 5.33mm for camera #4).

The cloud-to-cloud distance metric yields similar findings to those obtained using the camera-to-cloud metric, which confirms the applicability of the proposed system in an intensive care environment. Furthermore, the camera can be placed at both top and bottom positions of the patient's bed.

TABLE 3. System accuracy when changing the sensor positions using the cloud-to-camera metric (over one minute).

Experiment Number		#1	#2	#3	#4
Mode		Normal	Mild	Severe	Irregular
Reference camera	Δd_{camera} (cm)	0,23±0,13	1,95 ±0,24	3,64±0,41	2,77±0,11
Camera 1	Δd (cm)	0,26±0,21	1,92 ±0,19	3,59±0,59	2,74±0,34
	ρ	0,994	0.991	0,993	0.989
	$RMSD$ (mm)	2.23	2.53	2.317	2.814
Camera 2	Δd (cm)	0,24±0,34	1,94 ±0,32	3,62±0,17	2,76±0,25
	ρ	0,988	0.99	0,981	0.984
	$RMSD$ (mm)	2.0684	2.0387	2.1502	2.5196
Camera 3	Δd (cm)	0,45±0,48	2,36 ±0,44	4,21±0,64	3,01±0,75
	ρ	0.9673	0.9549	0,9625	0.9639
	$RMSD$ (mm)	3.78	4.83	5.23	6.34
Camera 4	Δd (cm)	0,33±0,13	2,11 ±0,24	4,71±0,41	2,97±0,64
	ρ	0,9532	0.9743	0.9627	0.9471
	$RMSD$ (mm)	5.16	4.94	6.64	6.38

TABLE 4. System accuracy when changing the sensor positions using the cloud-to-cloud metric (over one minute).

Experiment Number		#1	#2	#3	#4
Mode		Normal	Mild	Severe	Irregular
Reference camera	Δd_{camera} (cm)	0,34±0,316	2,24 ±0,346	3,94±0,649	2,91±0,216
Camera 1	Δd (cm)	0,36±0,78	2,12 ±0,45	3,99±0,32	3,11±0,64
	ρ	0,992	0.991	0,992	0.99
	$RMSD$ (mm)	2.316	2.612	2.346	2.914
Camera 2	Δd (cm)	0,34±0,62	2,33 ±0,15	3,96±0,34	2,9±0,56
	ρ	0,992	0.992	0,989	0.99
	$RMSD$ (mm)	2.157	2.364	2.316	2.846
Camera 3	Δd (cm)	0,42±0,67	2,75 ±0,54	4,98±0,41	3,67±0,74
	ρ	0.988	0.991	0,987	0.97
	$RMSD$ (mm)	5.87	5.64	6.15	6.29
Camera 4	Δd (cm)	0,31±0,35	2,66 ±0,43	4,34±0,51	3,03±0,72
	ρ	0,981	0.986	0.969	0.963
	$RMSD$ (mm)	5.74	5.34	4.12	6.12

However, placing the camera at the top of the bed yields slightly better results. The slight difference in performance between top and bottom positions is due to the camera depth resolution, which varies with distance from the sensor [55], [63]. Nevertheless, the accuracy in the bottom position is considered acceptable for the calculation of the retraction distance.

Our proposed system offers a new innovative method allowing not only the detection of respiratory failure in spontaneous breathing patients but also the visualization and quantification of the severity degree of TAA in patients with respiratory failure. This should have a great clinical impact and potential to improve respiratory management, especially when healthcare resources such as pediatric expert are limited.

Although the mannequin-based simulator system is high fidelity and provides the correct chest wall geometry and motion in TAA patients, some issues related to the realism of the phantom-based simulator may limit the actual clinical application of our findings. The first potential issue is related to the shortcomings of the mannequin's physical signs and the lack of an investigation of real patient's response to the system. The mannequin is mainly programmed to reproduce the asynchronous thoraco-abdominal motion in spontaneous breathing patients. The system performance should be investigated in real patients, and more specifically in the pediatric population given their overall low degree of cooperation. Some situations may affect the assumptions under which the reported performance has been achieved. These include the infant's increased stress, augmented anxiety/agitation and infant movement beyond the system's field of view. The second potential issue lies in the scope of real clinical situations management, including the cases of: occlusion by a nurse/health professional; a patient's change in position and any obscuration by bed clothing or bed sheets.

In view of the limitations regarding real subjects in a real clinical environment, it is important to frame the context of this study in order to more fully understand some assumptions and conditions. This improved understanding will make it possible to realize the system's optimal performance.

The initial assessment of an infant in respiratory failure is aimed first at the detection of a potential respiratory failure

and then at it's the degree of severity degree. This assessment will allow the patient to be managed promptly with immediate oxygen support or even intubation and mechanical ventilation. The proposed system is intended to improve the scope of the clinical decision-support tools.

In this regard, the measuring process can be intermittent or sequential; it does not necessarily need to be continuous. Indeed, measuring the retraction distance between the thorax and the abdomen is carried out at regular intervals, which are defined by relevant health care staff. Therefore, our camera based-system is highly appropriate for spontaneous breathing assessment in intensive care environments as our method can successfully measure the relevant parameters from a short acquisition where there is no occlusion. The medical examination is carried out on naked torso patients in a supine position and in intermittent operation mode without interfering with day-to-day procedures. This approach prevents a potential occlusion by a nurse/health professional or any obscuration by bed clothing or bed sheets. It is therefore essential to respect these conditions over which the optimal system operation is achieved (patient in supine position, patient with naked torso, avoid occlusions when acquiring data). The intermittent nature of assessment in a spontaneous breathing patient clearly facilitates compliance with these optimal conditions.

Addressing all possible TAA modes was made possible through this pilot study by using a high-fidelity phantom designed according to the human chest wall deformity characteristics. The hospital procedure requires the simulation of new clinical systems before they can be used in real situations.

Future works will mainly focus on performing experiments on patients as well as on phantoms to complement our initial findings, and to set out the system in a clinical environment to be used in a daily routine practice. We plan to evaluate the system using different kinds of clothing (sweater, T-shirt, pajamas...) and study how garments may affect the accuracy of measurements. For other future studies, we plan to build a reference TAA dataset using our video recordings. This will pave the way for this line of research. Our method allows detecting, visualizing and quantifying the thoraco-abdominal asynchrony. The system's ability will be extended by defining and training a deep neural network model with the future TAA dataset, thereby improving the automatic classification of illness severity.

VI. CONCLUSION

This manuscript presents a new non-contact vision-based method for monitoring acute respiratory failure in a pediatric intensive care environment. The proposed system uses a depth sensor to track the thoracic and abdominal surface motion with high spatial and temporal resolutions. A 3D motion field is computed for each time frame using the collected RGB-D data.

This is the first objective method to be proposed for the assessment of retraction signs. The results confirm the accuracy of the proposed method in the estimation of retraction zone distance with a significant agreement with a laser distance sensor system. The accuracy is slightly better in the bed head positions than at the bottom positions due to the hardware's limitation.

Our system is a very promising support tool intended to assist caregivers in respiration assessment in a pediatric intensive care environment. For future work, we aim to design a fully integrated and straightforward system for respiration assessment. In a previous work, we developed a system that estimates the most relevant respiratory parameters in PICU: tidal volume, respiratory rate, minute ventilation and inspiratory time. We plan to merge and simplify the two techniques so they will function in a single straightforward measurement system.

REFERENCES

[1] H. Aly, "Respiratory disorders in the newborn: Identification and diagnosis," *Pediatrics Rev.*, vol. 25, no. 6, pp. 201–208, 2004.

[2] Y. Sivan, T. W. Deakers, and C. J. L. Newth, "Thoracoabdominal asynchrony in acute upper airway obstruction in small children," *Amer. Rev. Respiratory Disease*, vol. 142, pp. 540–544, Sep. 1990.

[3] J. Hammer and C. J. L. Newth, "Assessment of thoraco-abdominal asynchrony," *Paediatric Respiratory Rev.*, vol. 10, no. 2, pp. 75–80, 2009.

[4] J. A. Verschakelen and M. G. Demedts, "Normal thoracoabdominal motions. Influence of sex, age, posture, and breath size.," *Amer. J. Respiratory Crit. Care Med.*, vol. 151, no. 2, pp. 399–405, 1995.

[5] M. J. Tobin, T. S. Chadha, G. Jenouri, S. J. Birch, H. B. Gazeroglu, and M. A. Sackner, "Breathing patterns: 2. Diseased subjects," *Chest*, vol. 84, no. 3, pp. 286–294, 1983.

[6] E. Bar-Yishay, A. Putilov, and S. Einav, "Automated, real-time calibration of the respiratory inductance plethysmograph and its application in newborn infants," *Physiol. Meas.*, vol. 24, no. 1, p. 149, 2003.

[7] M. J. Tobin, T. S. Chadha, G. Jenouri, S. J. Birch, H. B. Gazeroglu, and M. A. Sackner, "Breathing patterns: 1. Normal subjects," *Chest*, vol. 84, no. 2, pp. 202–205, 1983.

[8] R. Gilbert, J. H. Auchincloss, Jr., and D. Peppi, "Relationship of rib cage and abdomen motion to diaphragm function during quiet breathing," *Chest*, vol. 80, no. 5, pp. 607–612, 1981.

[9] J. T. Sharp, N. B. Goldberg, W. S. Druz, and J. Danon, "Relative contributions of rib cage and abdomen to breathing in normal subjects," *J. Appl. Physiol.*, vol. 39, no. 4, pp. 608–618, 1975.

[10] B. Binazzi, B. Lanini, R. Bianchi, I. Romagnoli, M. Nerini, F. Gigliotti, R. Duranti, J. Milic-Emili, and G. Scano, "Breathing pattern and kinematics in normal subjects during speech, singing and loud whispering," *Acta Physiol.*, vol. 186, no. 3, pp. 233–246, 2006.

[11] M. Romei, A. Lo Mauro, M. G. D'angelo, A. C. Turconi, N. Bresolin, A. Pedotti, and A. Aliverti, "Effects of gender and posture on thoraco-abdominal kinematics during quiet breathing in healthy adults," *Respiratory Physiol. Neurobiol.*, vol. 172, no. 3, pp. 184–191, 2010.

[12] S. J. Cala, C. M. Kenyon, G. Ferrigno, P. Carnevali, A. Aliverti, A. Pedotti, P. T. Macklem, and D. F. Rochester, "Chest wall and lung volume estimation by optical reflectance motion analysis," *J. Appl. Physiol.*, vol. 81, no. 6, pp. 2680–2689, 1996.

[13] A. Aliverti, R. L. Dellaca, P. Pelosi, D. Chiumello, A. Pedotti, and L. Gattinoni, "Optoelectronic plethysmography in intensive care patients," *Amer. J. Respiratory Crit. Care Med.*, vol. 161, no. 5, pp. 1546–1552, May 2000.

[14] A. Aliverti, R. Dellacà, P. Pelosi, D. Chiumello, L. Gattinoni, and A. Pedotti, "Compartmental analysis of breathing in the supine and prone positions by optoelectronic plethysmography," *Ann. Biomed. Eng.*, vol. 29, no. 1, pp. 60–70, 2001.

[15] T. Kondo, I. Kobayashi, Y. Taguchi, Y. Ohta, and N. Yanagimachi, "A dynamic analysis of chest wall motions with MRI in healthy young subjects," *Respirology*, vol. 5, no. 1, pp. 19–25, 2000.

[16] E. G. Culham, H. A. Jimenez, and C. E. King, "Thoracic kyphosis, rib mobility, and lung volumes in normal women and women with osteoporosis." *Spine*, vol. 19, no. 11, pp. 1250–1255, 1994.

[17] R. L. Dellaca, M. L. Ventura, E. Zannin, M. Natile, A. Pedotti, and P. Tagliabue, "Measurement of total and compartmental lung volume changes in newborns by optoelectronic plethysmography," *Pediatric Res.*, vol. 67, no. 1, pp. 11–16, 2010.
[18] M. C. Pereira, D. C. Porras, A. C. Lunardi, C. C. B. M. da Silva, R. C. C. Barbosa, L. Z. Cardenas, R. Pletsch, J. G. Ferreira, I. de Castro, C. R. F. de Carvalho, P. Caruso, C. R. R. de Carvalho, and A. L. P. de Albuquerque, "Thoracoabdominal asynchrony: Two methods in healthy, COPD, and interstitial lung disease patients," *PLoS ONE*, vol. 12, no. 8, 2017, Art. no. e0182417.
[19] A. Aliverti and A. Pedotti, "Opto-electronic plethysmography," in *Mechanics of Breathing*. Milano, Italy: Springer, 2002, pp. 47–59.
[20] C. M. A. Reinaux, A. Aliverti, L. G. M. da Silva, R. J. da Silva, J. N. Gonçalves, J. B. Noronha, J. E. C. Filho, A. D. de Andrade, and M. C. de Amorim Britto, "Tidal volume measurements in infants: Opto-electronic plethysmography versus pneumotachograph," *Pediatric Pulmonol.*, vol. 51, no. 8, pp. 850–857, 2016.
[21] Y. Zhang, J. Yang, L. Zhang, L. E. Court, P. A. Balter, and L. Dong, "Modeling respiratory motion for reducing motion artifacts in 4D CT images," *Med. Phys.*, vol. 40, no. 4, 2013, Art. no. 41716.
[22] F. Tahavori, M. Alnowami, and K. Wells, "Marker-less respiratory motion modeling using the microsoft Kinect for windows," *Proc. SPIE*, vol. 9036, Mar. 2014, Art. no. 90360K.
[23] C. Ozhasoglu and M. J. Murphy, "Issues in respiratory motion compensation during external-beam radiotherapy," *Int. J. Radiat. Oncol. Biol. Phys.*, vol. 52, no. 5, pp. 1389–1399, 2002.
[24] B. Nutti, Å. Kronander, M. Nilsing, K. Maad, C. Svensson, and H. Li, "Depth sensor-based realtime tumor tracking for accurate radiation therapy," in *Eurographics* (Short Papers). Strasbourg, France: Eurographics Association, 2014, pp. 1–4.
[25] P. Henry, M. Krainin, E. Herbst, X. Ren, and D. Fox, "RGB-D mapping: Using depth cameras for dense 3D modeling of indoor environments," in *Experimental Robotics*. Berlin, Germany: Springer, 2014, pp. 477–491.
[26] H. Aoki, M. Miyazaki, H. Nakamura, R. Furukawa, R. Sagawa, and H. Kawasaki, "Non-contact respiration measurement using structured light 3-D sensor," in *Proc. SICE Annu. Conf. (SICE)*, 2012, pp. 614–618.
[27] M. R. Alnowam, E. Lewis, K. Wells, and M. Guy, "Respiratory motion modelling and prediction using probability density estimation," in *Proc. IEEE Nucl. Sci. Symp. Med. Imag. Conf. (NSS/MIC)*, Oct./Nov. 2010, pp. 2465–2469.
[28] F. Benetazzo, A. Freddi, A. Monteriù, and S. Longhi, "Respiratory rate detection algorithm based on RGB-D camera: Theoretical background and experimental results," *Healthcare Technol. Lett.*, vol. 1, no. 3, pp. 81–86, 2014.
[29] A. Procházka, M. Schätz, O. Vyšata, and M. Vališ, "Microsoft Kinect visual and depth sensors for breathing and heart rate analysis," *Sensors*, vol. 16, no. 12, p. 996, Jun. 2016.
[30] V. Soleimani, M. Mirmehdi, D. Damen, J. Dodd, S. Hannuna, C. Sharp, M. Camplani, and J. Viner, "Remote, depth-based lung function assessment," *IEEE Trans. Biomed. Eng.*, vol. 64, no. 8, pp. 1943–1958, Aug. 2017.
[31] C. Sharp, V. Soleimani, S. Hannuna, M. Camplani, D. Damen, J. Viner, M. Mirmehdi, and J. W. Dodd, "Toward respiratory assessment using depth measurements from a time-of-flight sensor," *Frontiers Physiol.*, vol. 8, p. 65, Feb. 2017.
[32] H. Rehouma, R. Noumeir, W. Bouachir, P. Jouvet, and S. Essouri, "3D imaging system for respiratory monitoring in pediatric intensive care environment," *Comput. Med. Imag. Graph.*, vol. 70, pp. 17–28, Dec. 2018.
[33] T. M. Seppänen, J. Kananen, K. Noponen, O.-P. Alho, and T. Seppänen, "Accurate measurement of respiratory airflow waveforms using depth data," in *Proc. 37th Annu. Int. Conf. IEEE Eng. Med. Biol. Soc. (EMBC)*, Aug. 2015, pp. 7857–7860.
[34] K. Povšič, M. Jezeršek, and J. Možina, "Real-time 3D visualization of the thoraco-abdominal surface during breathing with body movement and deformation extraction," *Physiol. Meas.*, vol. 36, no. 7, p. 1497, 2015.
[35] M. Heß, F. Büther, F. Gigengack, M. Dawood, and K. P. Schäfers, "A dual-Kinect approach to determine torso surface motion for respiratory motion correction in PET," *Med. Phys.*, vol. 42, no. 5, pp. 2276–2286, 2015.
[36] C. Ulrich, C. Schaller, J. Penne, and J. Hornegger, "Evaluation of a time-of-flight-based respiratory motion management system," in *Bildverarbeitung für die Medizin*. Aachen, Germany: Springer, 2010, pp. 152–156.
[37] J. Penne, C. Schaller, J. Hornegger, and T. Kuwert, "Robust real-time 3D respiratory motion detection using time-of-flight cameras," *Int. J. Comput. Assist. Radiol. Surg.*, vol. 3, no. 5, pp. 427–431, Nov. 2008.
[38] D. Falie, M. Ichim, and L. David, "Respiratory motion visualization and the sleep apnea diagnosis with the time of flight (ToF) camera," in *Visualisation, Imaging and Simulation*. Bucharest, Romania: World Scientific and Engineering Academy and Society, 2008.
[39] C. Schaller, J. Penne, and J. Hornegger, "Time-of-flight sensor for respiratory motion gating," *Med. Phys.*, vol. 35, no. 7Part1, pp. 3090–3093, 2008.
[40] W. de Boer, "SLP: A zero-contact non-invasive method for pulmonary function testing." in *Proc. BMVC*, 2010, pp. 1–12.
[41] M.-C. Yu, J.-L. Liou, S.-W. Kuo, M.-S. Lee, and Y.-P. Hung, "Noncontact respiratory measurement of volume change using depth camera," in *Proc. Annu. Int. Conf. IEEE Eng. Med. Biol. Soc.*, Aug./Sep. 2012, pp. 2371–2374.
[42] S. Ostadabbas, C. Bulach, D. N. Ku, L. J. Anderson, and M. Ghovanloo, "A passive quantitative measurement of airway resistance using depth data," in *Proc. 36th Annu. Int. Conf. IEEE Eng. Med. Biol. Soc.*, Aug. 2014, pp. 5743–5747.
[43] G. Li, H. Huang, J. Wei, D. G. Li, Q. Chen, C. P. Gaebler, J. Sullivan, J. Zatcky, A. Rimner, and J. Mechalakos, "Novel spirometry based on optical surface imaging," *Med. Phys.*, vol. 42, no. 4, pp. 1690–1697, 2015.
[44] S. Ostadabbas, N. Sebkhi, M. Zhang, S. Rahim, L. J. Anderson, F. E.-H. Lee, and M. Ghovanloo, "A vision-based respiration monitoring system for passive airway resistance estimation," *IEEE Trans. Biomed. Eng.*, vol. 63, no. 9, pp. 1904–1913, Sep. 2016.
[45] A. Procházka, M. Schätz, O. Vyšata, and M. Vališ, "Microsoft Kinect visual and depth sensors for breathing and heart rate analysis," *Sensors*, vol. 16, no. 7, p. 996, 2016.
[46] E. J. Sirevaag, S. Casaccia, E. A. Richter, J. A. O'Sullivan, L. Scalise, and J. W. Rohrbaugh, "Cardiorespiratory interactions: Noncontact assessment using laser Doppler vibrometry," *Psychophysiology*, vol. 53, no. 6, pp. 847–867, 2016.
[47] J. E. Gern, M. S. Martin, K. A. Anklam, K. Shen, K. A. Roberg, K. T. Carlson-Dakes, K. Adler, S. Gilbertson-White, R. Hamilton, P. A. Shult, C. J. Kirk, D. F. Da Silva, S. A. Sund, M. R. Kosorok, and R. F. Lemanske, Jr., "Relationships among specific viral pathogens, virus-induced interleukin-8, and respiratory symptoms in infancy," *Pediatric Allergy Immunol.*, vol. 13, no. 6, pp. 386–393, 2002.
[48] J. O. Wishaupt, E. A. N. van den Berg, T. van Wijk, T. van der Ploeg, F. G. A. Versteegh, and N. G. Hartwig, "Paediatric apnoeas are not related to a specific respiratory virus, and parental reports predict hospitalisation," *Acta Paediatrica*, vol. 105, no. 5, pp. 542–548, 2016.
[49] G. M. Davis, D. M. Cooper, and I. Mitchell, "The measurement of thoraco-abdominal asynchrony in infants with severe laryngotracheobronchitis," *Chest*, vol. 103, no. 6, pp. 1842–1848, 1993.
[50] S. L. Balasubramaniam, Y. Wang, L. Ryan, J. Hossain, T. Rahman, and T. H. Shaffer, "Age-related ranges of respiratory inductance plethysmography (RIP) reference values for infants and children," *Paediatric Respiratory Rev.*, vol. 29, pp. 60–67, Feb. 2019.
[51] A. Maizels, A. Shpunt, and S. Litvak, "Enhanced 3d interfacing for remote devices," U.S. Patent 20 100 235 786 A1, Sep. 16, 2010.
[52] H. Sarbolandi, D. Lefloch, and A. Kolb, "Kinect range sensing: Structured-light versus time-of-flight Kinect," *Comput. Vis. Image Understand.*, vol. 139, pp. 1–20, Oct. 2015.
[53] C. D. Mutto, P. Zanuttigh, and G. M. Cortelazzo, *Time-of-Flight Cameras and Microsoft Kinect (TM)*. New York, NY, USA: Springer, 2012.
[54] T. Mallick, P. P. Das, and A. K. Majumdar, "Characterizations of noise in Kinect depth images: A review," *IEEE Sensors*, vol. 14, no. 6, pp. 1731–1740, Jun. 2014.
[55] K. Khoshelham and S. O. Elberink, "Accuracy and resolution of Kinect depth data for indoor mapping applications," *Sensors*, vol. 12, no. 2, pp. 1437–1454, Feb. 2012.
[56] E. Lachat, H. Macher, T. Landes, and P. Grussenmeyer, "Assessment and calibration of a RGB-D camera (Kinect v2 sensor) towards a potential use for close-range 3D modeling," *Remote Sens.*, vol. 7, no. 10, pp. 13070–13097, 2015.
[57] S. T. L. Pöhlmann, E. F. Harkness, C. J. Taylor, and S. M. Astley, "Evaluation of Kinect 3d sensor for healthcare imaging," *J. Med. Biol. Eng.*, vol. 36, no. 6, pp. 857–870, 2016.
[58] B. K. P. Horn and B. G. Schunck, "Determining optical flow," *Artif. Intell.*, vol. 17, nos. 1–3, pp. 185–203, Aug. 1981.
[59] L. L. Tarnec, F. Destrempes, G. Cloutier, and D. Garcia, "A proof of convergence of the Horn–Schunck optical flow algorithm in arbitrary dimension," *SIAM J. Imag. Sci.*, vol. 7, no. 1, pp. 277–293, 2014.
[60] M. Jaimez, M. Souiai, J. Gonzalez-jimenez, and D. Cremers, "A primal-dual framework for real-time dense RGB-D scene flow," in *Proc. IEEE Int. Conf. Robot. Automat. (ICRA)*, May 2015, pp. 98–104.

[61] P. Merat, E. J. Harvey, and G. D. Mitsis, "A miniature multi-sensor shoe-mounted platform for accurate positioning," in *Proc. IEEE Int. Conf. Syst., Man, Cybern. (SMC)*, Oct. 2018, pp. 2772–2777.
[62] Z. Chen, Y. Wang, and H. Liu, "Unobtrusive sensor-based occupancy facing direction detection and tracking using advanced machine learning algorithms," *IEEE Sensors J.*, vol. 18, no. 15, pp. 6360–6368, Aug. 2018.
[63] C. Nock, O. Taugourdeau, S. DeLagrange, and C. Messier, "Assessing the potential of low-cost 3D cameras for the rapid measurement of plant woody structure," *Sensors*, vol. 13, no. 12, pp. 16216–16233, 2013.

HAYTHEM REHOUMA received the bachelor's degree in telecommunications and the M.Sc. degrees in communications systems (SysCom) from the National Engineering School of Tunis (ENIT), Tunis, Tunisia, in 2010 and 2011, respectively. He is currently pursuing the Ph.D. degree in 3-D imaging and biomedical signal processing and instrumentation with the Biomedical Information Processing Laboratory, École De Technologie Supérieure, University of Quebec, Montreal, QC, Canada. He is also an Associate Researcher and a Software Programming Teacher with the Department of Electrical Engineering. His research interests include technologies, intelligent systems, and models for next-generation health monitoring techniques, with a focus on respiratory assessment using computer vision algorithms.

RITA NOUMEIR received the M.Sc. and Ph.D. degrees in biomedical engineering from the École Polytechnique, University of Montreal. She is currently a Professor with the Electrical Engineering Department, École de Technologie Supérieure (ETS), University of Quebec, Montreal, QC, Canada. She has been actively involved with IHE since its inception. As a member of the Radiology IHE Planning Committee, she has been involved in establishing the broad direction and scope for the IHE demonstrations and in planning IHE workshops and other activities. She presented IHE at various international conferences and workshops. As a member of the Radiology IHE Technical Committee, she has participated in developing the IHE integration profiles that are detailed in the actual IHE technical framework. She has written numerous articles in biomedical informatics. She has published and lectured extensively in software analysis and image processing and participated in launching the new software engineering program at ETS. She has provided consulting services, including architecture analysis, workflow analysis, technology assessment, and image processing for several software and medical companies.

GABRIEL MASSON received the M.D. degree specialty in anesthesiology from Lille University, in 2015, where he is currently pursuing the M.D. degree subspecialty in intensive care. Simultaneously he is also pursuing the M.Sc. degree in biomedical research from the University of Lille in collaboration with the Sainte Justine Hospital–University of Montreal. He is also a part of few research programs on computerized decision support systems and evaluation of the work of breathing in pediatric and adult patients. His research program is supported by several grants from Sainte-Justine Hospital, Lille University Hospital, and the French Intensive Care Society. He is also a member of the Scientific Advisory Committee of three French medical congresses in the field of anesthesia and intensive care.

SANDRINE ESSOURI received the M.D. degree specialty in Pediatrics and subspecialty in intensive care from Paris VII University, in 2000, and the Ph.D. degree in physiology and physiopathology of the hemodynamic and respiratory systems from Paris XII University, in 2007. She joined the Pediatric Unit of Sainte Justine Hospital–University of Montreal, in 2015. She is currently a part of few research programs on computerized decision support systems for health providers and evaluation of the work of breathing in pediatric patient with acute respiratory failure. Her research program is supported by several grants from Sainte-Justine Hospital, Quebec ministry of Health, and the Réseau en Santé Respiratoire (RSR). She has published more than 45 articles in peer-reviewed journals and gave more than 40 lectures in national and international congresses.

PHILIPPE JOUVET received the M.D. degree specialty in pediatrics and subspecialty in intensive care from Paris V University, in 1989, and the Ph.D. degree in pathophysiology of human nutrition and metabolism from Paris VII University, in 2001. He joined the Pediatric Intensive Care Unit of Sainte Justine Hospital–University of Montreal, in 2004. He is currently the Deputy Director of the Research Center and the Scientific Director of the Health Technology Assessment Unit of the Sainte Justine Hospital–University of Montreal. He has a salary award for research from the Quebec public research agency (FRQS). He also conducts a research program on computerized decision support systems for health providers. His research program is supported by several grants from Sainte-Justine Hospital, Quebec Ministry of Health, the FRQS, Canadian Institutes of Health Research (CIHR), and the Natural Sciences and Engineering Research Council (NSERC). He has published more than 160 articles in peer reviewed journals and gave more than 120 lectures in national and international congresses.